Hindawi
Advances in Materials Science and Engineering
Volume 2020, Article ID 3618984, 17 pages
https://doi.org/10.1155/2020/3618984

Research Article

Effect of Interface Properties on Tensile and Fatigue Behavior of 2D Woven SiC/SiC Fiber-Reinforced Ceramic-Matrix Composites

Longbiao Li

College of Civil Aviation, Nanjing University of Aeronautics and Astronautics, No. 29 Yudao St., Nanjing 210016, China

Correspondence should be addressed to Longbiao Li; llb451@nuaa.edu.cn

Received 14 November 2019; Accepted 17 December 2019; Published 8 January 2020

Academic Editor: Luigi Nicolais

In this paper, the effect of the fiber/matrix interface properties on the tensile and fatigue behavior of 2D woven SiC/SiC ceramic-matrix composites (CMCs) is investigated. The relationships between the interface parameters of the fiber/matrix interface debonding energy and interface frictional shear stress in the interface debonding region and the composite tensile and fatigue damage parameters of first matrix cracking stress, matrix cracking density, and fatigue hysteresis-based damage parameters are established. The effects of the fiber/matrix interface properties on the first matrix cracking stress, matrix cracking evolution, first and complete interface debonding stress, fatigue hysteresis dissipated energy, hysteresis modulus, and hysteresis width are analyzed. The experimental first matrix cracking stress, matrix cracking evolution, and fatigue hysteresis loops of SiC/SiC composites are predicted using different interface properties.

1. Introduction

Ceramic matrix composites (CMCs) are widely used in the high-temperature field as a light and high-performance structural composite material. High-quality and high-temperature properties make it possible to replace superalloy materials as one of the candidate materials for aero-engines, especially for aero-engine core engines. In the research and application of CMCs, the existing mature aero-engines are fully utilized for assessment and verification from low temperature to high temperature, stator components to rotor components [1–6]. Firstly, the stator parts with medium temperature (700°C–1000°C) and medium load (less than 120 MPa) were developed, i.e., exhaust nozzle flaps and sealings; then the medium stator parts with high temperature (1000°C~1300°C) were developed, such as combustion chamber flame tube, flame stabilizer, turbine guide vane, and turbine outer ring; and the stator or rotor parts with higher load (more than 120 MPa), such as high-pressure turbine rotor and stator, have been developed [7–9]. The commercial aero-engines require low fuel consumption, low noise, and low NO_x emissions, so new requirements are put forward for pressure ratio and turbine front temperature. CMC has the characteristics of light weight, high-temperature resistance, corrosion resistance, and impact resistance, so it is expected to be used in combustion chambers, turbines, exhaust nozzles, and other components of the next generation of commercial aero-engines [10–12].

For fiber-reinforced CMCs, the mechanical properties depend tremendously on the load transfer at the fiber/matrix interface [13, 14]. The interface properties of the fiber/matrix interface shear stress and the interface debonding energy affect the tensile and fatigue behavior of fiber-reinforced CMCs [15–20]. Vagaggini et al. [21] developed an approach to establish the relationship between the interface properties and the hysteresis loops of fiber-reinforced CMCs and divided the interface debonding energy into small and large, which affects the shape of the hysteresis loops upon unloading and reloading. Domergue et al. [22] measured the interface properties of unidirectional SiC/CAS and SiC/SiC composites using the hysteresis loops, and the interface shear stress of SiC/SiC composite is much higher than that of SiC/CAS composite, leading to unsaturation of matrix cracking of SiC/SiC composite till tensile fracture. Curtin et al. [23] predicted the tensile stress-strain behavior of mini-SiC/SiC composite considering matrix cracking evolution, fiber damage, and

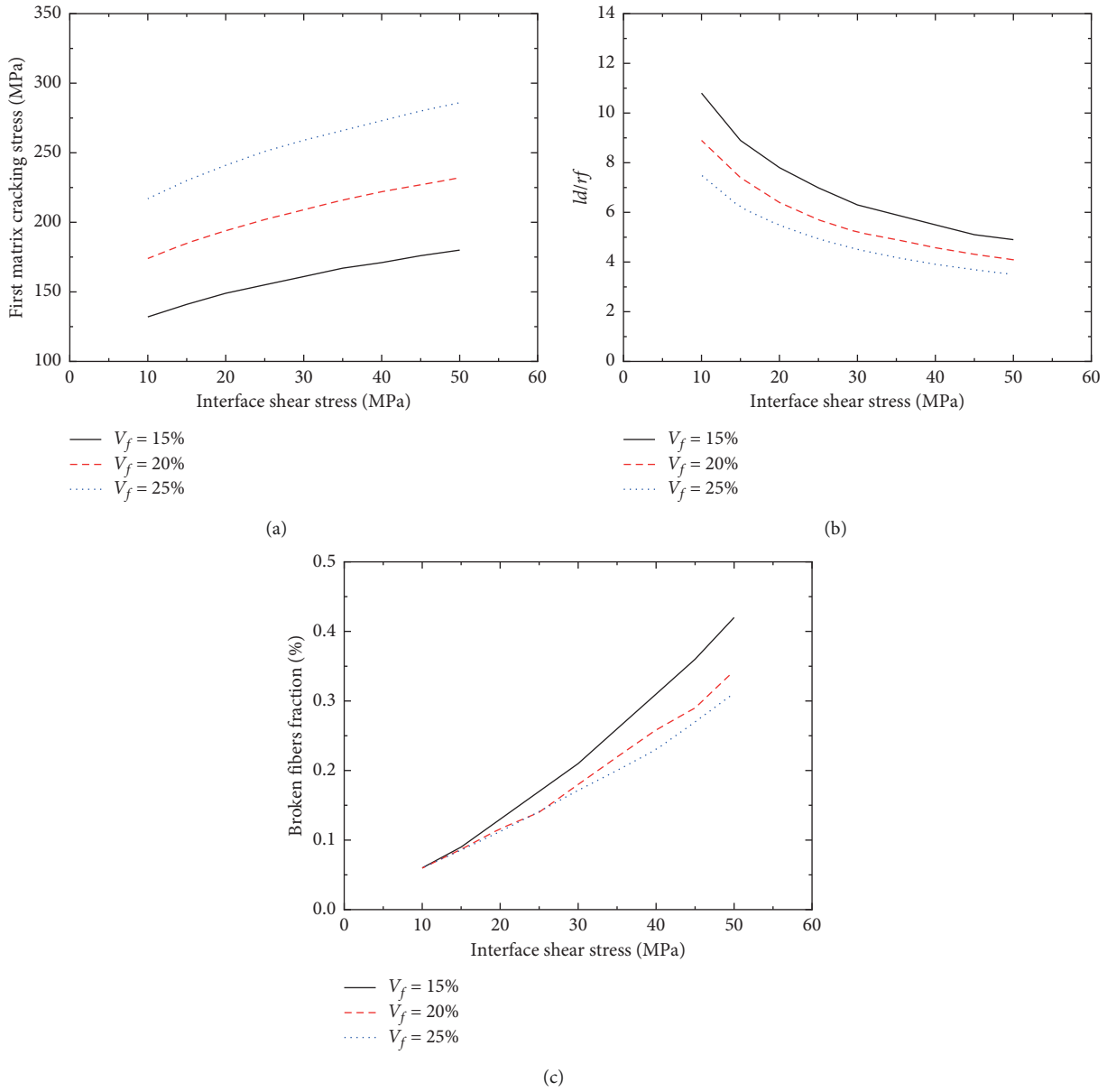

Figure 1: (a) The first matrix cracking stress versus the interface shear stress curves; (b) the interface debonding length versus the interface shear stress curves; (c) the broken fibers fraction versus the interface shear stress curves for different fiber volume.

ultimate failure. It was found that the matrix cracking stress affects the brittle and tough behavior of fiber-reinforced CMCs. Carrere et al. [24] investigated the influence of the interphase on the matrix cracking deflection in mini-SiC/C/SiC composite with a pyrocarbon interphase. The deflection of the matrix cracking depends on the interface bond strength between the fiber and the matrix. Xia and Curtin [25] investigated the high interface shear stress on the tensile strength of fiber-reinforced CMCs considering the stress concentration at the interface debonding tip. When the bond strength is high and the fiber/matrix interface frictional shear stress in the debonding region is low, the stress concentration occurs near the interface debonding tip. Sauder et al. [26] investigated the influence of the interface characteristics on the tensile and loading/unloading behavior of two different mini-SiC/SiC composites. The interphase thickness and the fiber surface roughness affect the fiber/matrix interface shear stress at the debonding region, and then the tensile behavior of fiber-reinforced CMCs. Under cyclic loading, the fiber/matrix interface shear stress decreases with applied cycles, which depends on the peak stress, stress ratio, loading frequency, temperature, and environment [27–35].

In this paper, the effect of the fiber/matrix interface properties on the tensile and fatigue behavior of 2D woven SiC/SiC composites is investigated. The relationships between the interface properties and the composite tensile and fatigue damage parameters are established. The effects of the interface properties on the first matrix cracking stress, matrix cracking evolution, first and complete interface debonding stress, fatigue hysteresis dissipated energy, fatigue hysteresis modulus,

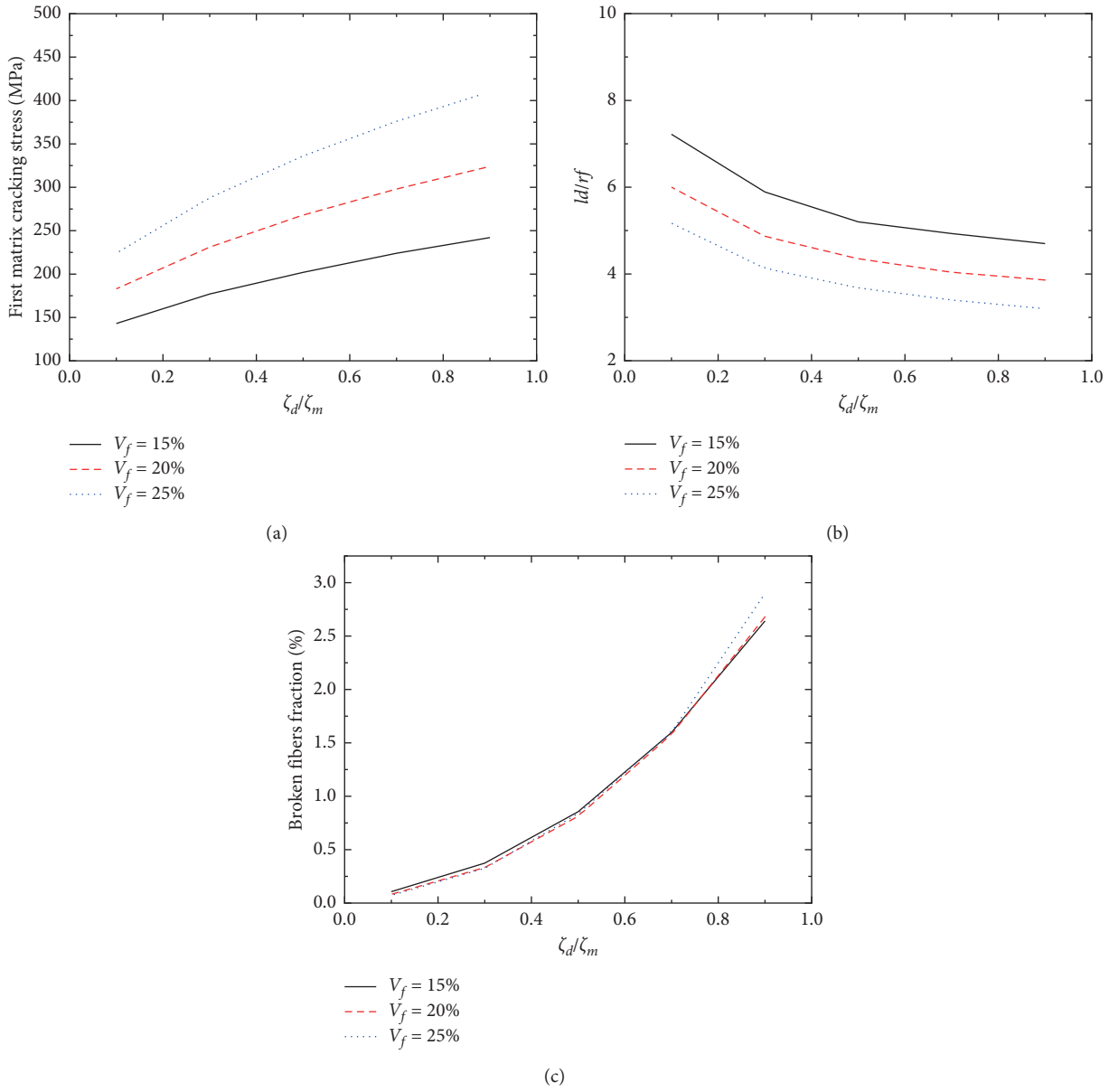

Figure 2: (a) The first matrix cracking stress versus the interface debonding energy curves; (b) the interface debonding length versus the interface debonding energy curves; (c) the broken fibers fraction versus the interface debonding energy curves for different fiber volume.

and fatigue hysteresis width are analyzed. The experimental tensile and fatigue behavior of SiC/SiC composites is predicted for different interface properties.

2. Theoretical Analysis

In the present analysis, the fiber failure is considered in the analysis of the first matrix cracking stress, matrix cracking density, interface debonding stress, and the fatigue hysteresis-based damage parameters.

2.1. First Matrix Cracking Stress. For the first matrix cracking of fiber-reinforced CMCs, the energy balance relationship can be determined as

$$\alpha\sigma^2 + \beta\sigma + \gamma = 0, \tag{1}$$

where

$$\begin{aligned}
\alpha &= \frac{l_d}{E_c}, \\
\beta &= -\frac{2V_f l_d T}{E_c}, \\
\gamma &= \frac{4}{3}\left(\frac{\tau_i}{r_f}\right)^2\left(\frac{V_f E_c}{V_m E_m E_f}\right)l_d^3 + \frac{V_f l_d T^2}{E_f} - \frac{2V_f \tau_i l_d^2}{r_f E_f}T \\
&\quad - V_m\zeta_m - \frac{4V_f l_d}{r_f}\zeta_d,
\end{aligned} \tag{2}$$

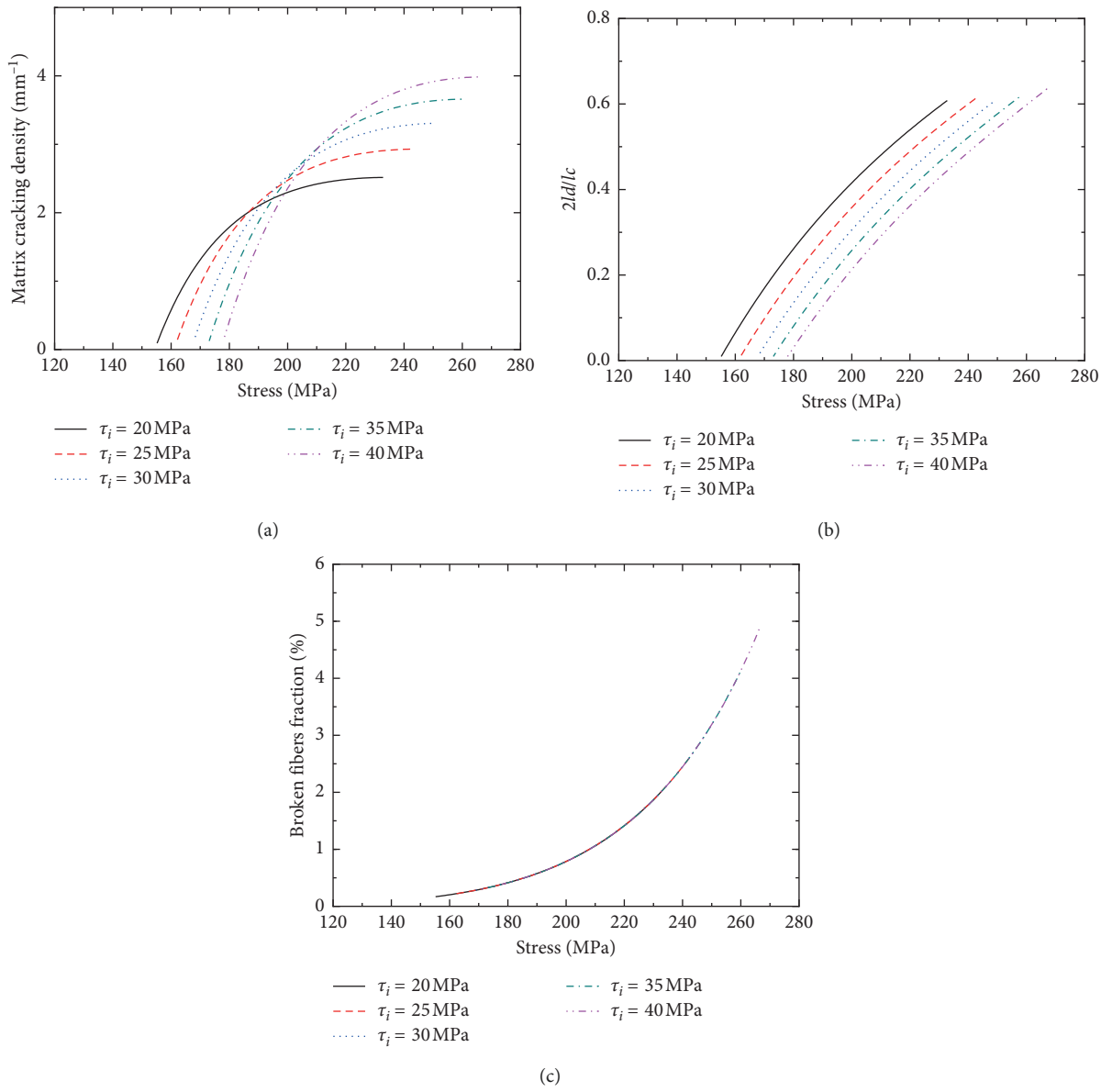

FIGURE 3: (a) The matrix cracking density versus the applied stress curves; (b) the interface debonding length versus the applied stress curves; (c) the broken fibers fraction versus the applied stress curves for different interface shear stress.

where l_d denotes the fiber/matrix interface debonding length; E_f, E_m, and E_c denote the fiber, matrix, and composite elastic modulus, respectively; V_f and V_m denote the fiber and the matrix volume, respectively; r_f denotes the fiber radius; ζ_m and ζ_d denote the matrix fracture energy and the interface debonding energy, respectively; τ_i denotes the fiber/matrix interface shear stress in the debonding region; and T denotes the fiber intact stress:

$$\frac{\sigma}{V_f} = T\left(\frac{\sigma_c}{T}\right)^{m+1}\left\{1 - \exp\left[-\left(\frac{T}{\sigma_c}\right)^{m+1}\right]\right\}, \quad (3)$$

where σ_c denotes the fiber characteristic strength and m denotes the fiber Weibull modulus.

2.2. Matrix Cracking Density. The energy balance relationship to evaluate the matrix cracking evolution is given by

$$U_m\left(\sigma > \sigma_{mc}, l_c, l_d\right) = U_{\text{crm}}\left(\sigma_{mc}, l_0\right), \quad (4)$$

where

$$U_m = \begin{cases} \dfrac{A_m}{E_m}\left\{\dfrac{4}{3}\left(\dfrac{V_f\tau_i}{V_m r_f}l_d\right)^2 l_d + \sigma_{mo}^2\left(\dfrac{l_c}{2}-l_d\right)\right. \\ \quad -2\sigma_{mo}\left[\dfrac{V_f}{V_m}\left(T-\sigma_{fo}\right)-2\dfrac{V_f\tau_i}{r_f V_m}l_d\right]\left(-\dfrac{r_f}{\rho}\right)\left[\exp\left(-\rho\dfrac{l_c/2-l_d}{r_f}\right)-1\right] \\ \quad \left.+\left[\dfrac{V_f}{V_m}\left(T-\sigma_{fo}\right)-2\dfrac{V_f\tau_i}{r_f V_m}l_d\right]^2\left(-\dfrac{r_f}{2\rho}\right)\left[\exp\left(-2\rho\dfrac{l_c/2-l_d}{r_f}\right)-1\right]\right\}, & l_d < \dfrac{l_c}{2}, \\ \dfrac{A_m l_c^3}{6E_m}\left(\dfrac{\tau_i V_f}{r_f V_m}\right)^2, & l_d = \dfrac{l_c}{2}, \end{cases} \tag{5}$$

$$U_{\text{crm}} = \frac{1}{2}kA_m l_0\frac{\sigma_{\text{mocr}}^2}{E_m},$$

where A_m is the cross-sectional area of matrix in the unit cell; k denotes the critical matrix strain energy parameter; l_0 is the initial matrix crack spacing; and σ_{mocr} denotes the matrix axial stress in the interface bonded region at the first matrix cracking stress.

2.3. Fatigue Hysteresis-Based Damage Parameters. The initial fiber/matrix interface debonding stress σ_d and the interface complete debonding stress σ_b can be obtained as

$$\begin{aligned} \sigma_d &= \frac{V_f E_c \tau_i}{\rho V_m E_m}\left[1+\sqrt{1+4\frac{V_m E_m E_f}{r_f E_c}\frac{\rho^2}{\tau_i^2}\zeta_d}\right], \\ \sigma_b &= \frac{V_f E_c \tau_i}{\rho V_m E_m}\left[1+\rho\frac{l_c}{r_f}+\sqrt{1+4\frac{V_m E_m E_f}{r_f E_c}\frac{\rho^2}{\tau_i^2}\zeta_d}\right]. \end{aligned} \tag{6}$$

The fatigue hysteresis dissipated energy U_e can be given by

$$U_e = \int_{\sigma_{\min}}^{\sigma_{\max}}\left[\varepsilon_{\text{unloading}}(\sigma)-\varepsilon_{\text{reloading}}(\sigma)\right]\mathrm{d}\sigma, \tag{7}$$

where

$$\varepsilon_{\text{unloading}} = \begin{cases} \dfrac{T_U}{E_f}+4\dfrac{\tau_i}{E_f}\dfrac{y^2}{r_f l_c}-\dfrac{\tau_i}{E_f}\dfrac{(2y-l_d)(2y+l_d-l_c)}{r_f l_c}-\left(\alpha_c-\alpha_f\right)\Delta\mathrm{T}, & l_d < \dfrac{l_c}{2}, \\ \dfrac{T_U}{E_f}+4\dfrac{\tau_i}{E_f}\dfrac{y^2}{r_f l_c}-2\dfrac{\tau_i}{E_f}\dfrac{(2y-l_c/2)^2}{r_f l_c}-\left(\alpha_c-\alpha_f\right)\Delta\mathrm{T}, & l_d = \dfrac{l_c}{2}, \end{cases}$$

$$\varepsilon_{\text{reloading}} = \begin{cases} \dfrac{T_R}{E_f}-4\dfrac{\tau_i}{E_f}\dfrac{z^2}{r_f l_c}+4\dfrac{\tau_i}{E_f}\dfrac{(y-2z)^2}{r_f l_c}+2\dfrac{\tau_i}{E_f}\dfrac{(l_d-2y+2z)(l_d+2y-2z-l_c)}{r_f l_c}-\left(\alpha_c-\alpha_f\right)\Delta\mathrm{T}, & l_d < \dfrac{l_c}{2}, \\ \dfrac{T_R}{E_f}-4\dfrac{\tau_i}{E_f}\dfrac{z^2}{r_f l_c}+4\dfrac{\tau_i}{E_f}\dfrac{(y-2z)^2}{r_f l_c}-2\dfrac{\tau_i}{E_f}\dfrac{(l_c/2-2y+2z)^2}{r_f l_c}-\left(\alpha_c-\alpha_f\right)\Delta\mathrm{T}, & l_d = \dfrac{l_c}{2}, \end{cases} \tag{8}$$

where T_U and T_R denote the intact fiber stress upon unloading and reloading, respectively.

The fatigue hysteresis width $\Delta\varepsilon$ can be given by

$$\Delta\varepsilon = \varepsilon_{\text{unloading}}\left(\frac{\sigma_{\min}+\sigma_{\max}}{2}\right)-\varepsilon_{\text{reloading}}\left(\frac{\sigma_{\min}+\sigma_{\max}}{2}\right). \tag{9}$$

The fatigue hysteresis modulus E can be obtained as

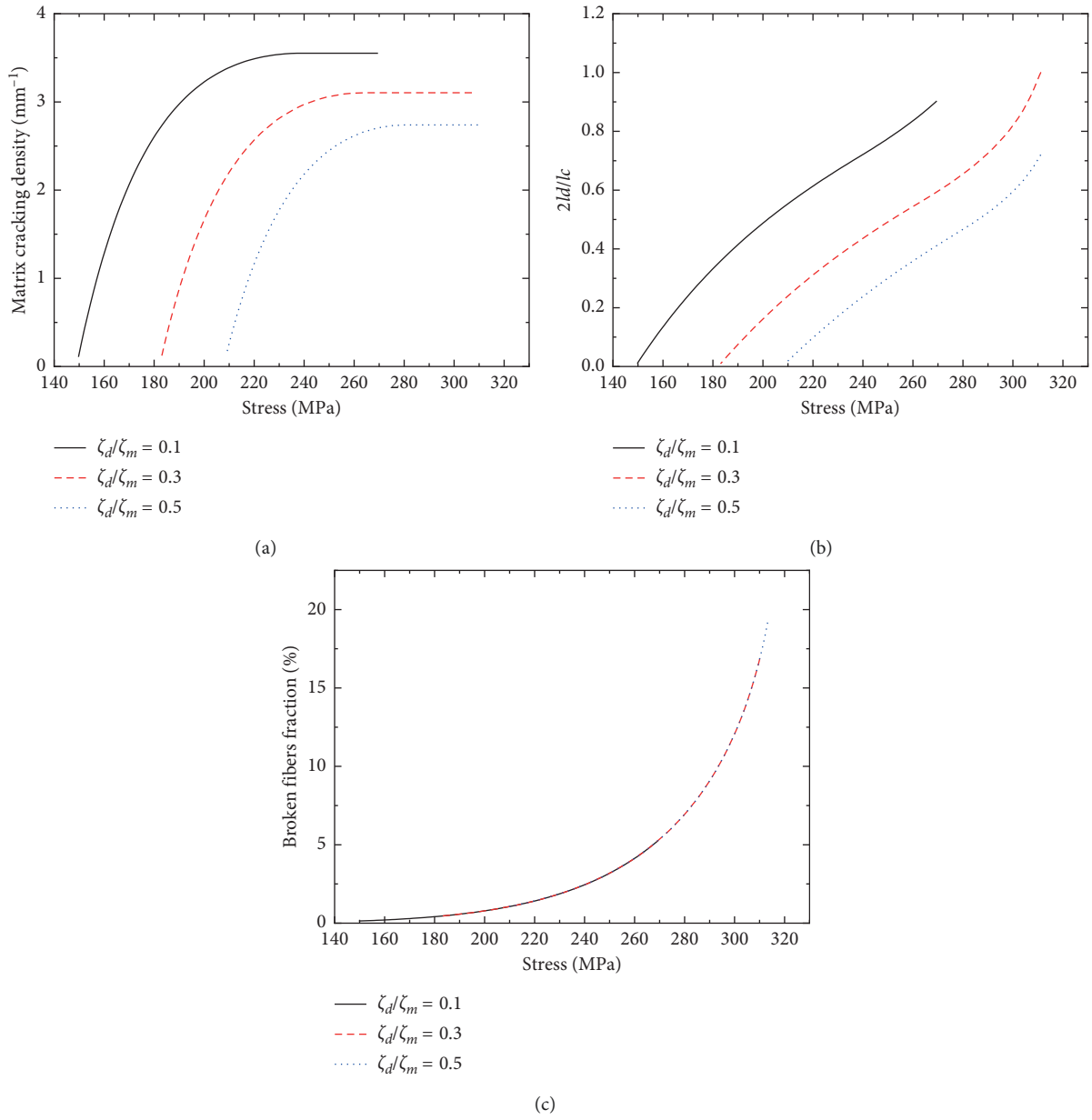

FIGURE 4: (a) The matrix cracking density versus the applied stress curves; (b) the interface debonding length versus the applied stress curves; (c) the broken fibers fraction versus the applied stress curves for different interface deboned energy.

$$E = \frac{\sigma_{\max} - \sigma_{\min}}{\varepsilon_{\max}(\sigma_{\max}) - \varepsilon_{\min}(\sigma_{\min})}. \quad (10)$$

3. Results and Discussion

The effects of fiber/matrix interface properties on the tensile and fatigue damage are analyzed. The SiC/SiC composite is used to the case analysis, and the material properties are given by $V_f = 15\%$, $E_f = 400$ GPa, $E_m = 350$ GPa, $r_f = 6\,\mu$m, $\alpha_f = 4.5 \times 10^{-6}/^{\circ}$C, $\alpha_m = 4.6 \times 10^{-6}/^{\circ}$C, $\Delta T = -1000^{\circ}$C, $\zeta_m = 6$ J/m^2, $\zeta_d = 1.2$ J/m^2, $\tau_i = 30$ MPa, $\sigma_c = 3.0$ GPa, and $m = 5$.

3.1. Effect of the Interface Properties on the First Matrix Cracking Stress. The first matrix cracking stress, the fiber/matrix interface debonding length, and broken fibers fraction versus the fiber/matrix interface shear stress and interface debonding energy curves for different fiber volume are shown in Figures 1 and 2. When the fiber/matrix interface shear stress and interface debonding energy increase, the first matrix cracking stress increases, the fiber/matrix interface debonding length decreases, and the broken fibers fraction increases.

When the fiber volume is $V_f = 15\%$, the first matrix cracking stress increases from $\sigma_{mc} = 132$ MPa at $\tau_i = 10$ MPa

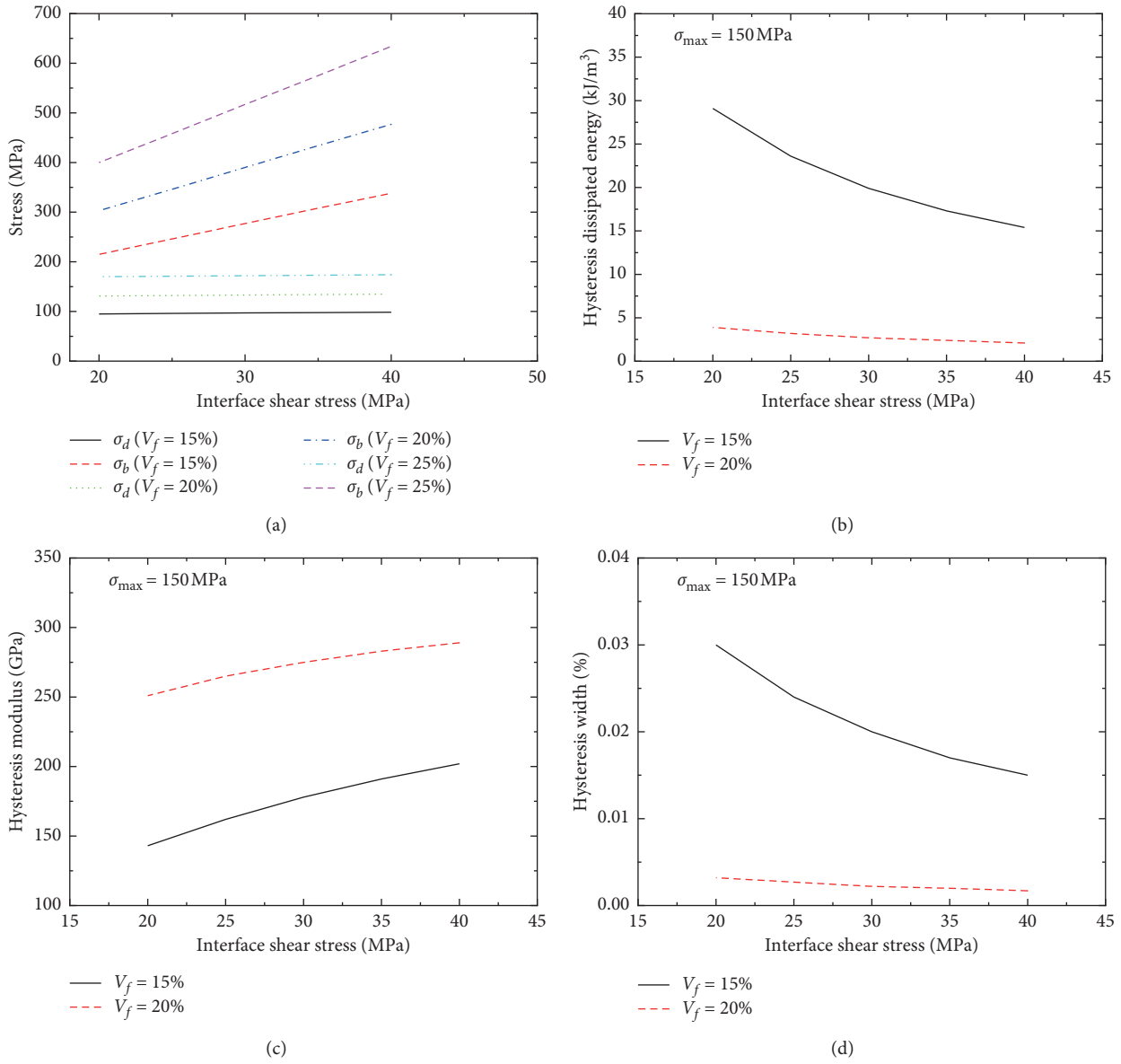

Figure 5: (a) The initial interface debonding stress and complete interface debonding stress versus the interface shear stress curves; (b) the fatigue hysteresis dissipated energy versus the interface shear stress curves; (c) the fatigue hysteresis modulus versus the interface shear stress curves; (d) the fatigue hysteresis width versus the interface shear stress curves for different fiber volume.

to $\sigma_{mc} = 180$ MPa at $\tau_i = 50$ MPa and from $\sigma_{mc} = 143$ MPa at $\zeta_d/\zeta_m = 0.1$ to $\sigma_{mc} = 242$ MPa at $\zeta_d/\zeta_m = 0.9$; the fiber/matrix interface debonding length decreases from $l_d/r_f = 10.8$ at $\tau_i = 10$ MPa to $l_d/r_f = 4.9$ at $\tau_i = 50$ MPa and from $l_d/r_f = 7.2$ at $\zeta_d/\zeta_m = 0.1$ to $l_d/r_f = 4.7$ at $\zeta_d/\zeta_m = 0.9$; and the broken fibers fraction increases from $q = 0.06\%$ at $\tau_i = 10$ MPa to $q = 0.42\%$ at $\tau_i = 50$ MPa and from $q = 0.1\%$ at $\zeta_d/\zeta_m = 0.1$ to $q = 2.6\%$ at $\zeta_d/\zeta_m = 0.9$.

When the fiber volume is $V_f = 25\%$, the first matrix cracking stress increases from $\sigma_{mc} = 217$ MPa at $\tau_i = 10$ MPa to $\sigma_{mc} = 286$ MPa at $\tau_i = 50$ MPa and from $\sigma_{mc} = 224$ MPa at $\zeta_d/\zeta_m = 0.1$ to $\sigma_{mc} = 410$ MPa at $\zeta_d/\zeta_m = 0.9$; the fiber/matrix interface debonding length decreases from $l_d/r_f = 7.5$ at $\tau_i = 10$ MPa to $l_d/r_f = 3.5$ at $\tau_i = 50$ MPa and from $l_d/r_f = 5.1$ at $\zeta_d/\zeta_m = 0.1$ to $l_d/r_f = 3.2$ at $\zeta_d/\zeta_m = 0.9$; and the broken fibers fraction increases from $q = 0.06\%$ at $\tau_i = 10$ MPa to $q = 0.31\%$ at $\tau_i = 50$ MPa and from $q = 0.07\%$ at $\zeta_d/\zeta_m = 0.1$ to $q = 2.9\%$ at $\zeta_d/\zeta_m = 0.9$.

3.2. Effect of the Interface Properties on the Matrix Cracking Density. The matrix cracking density, fiber/matrix interface debonding length, and broken fibers fraction versus the applied stress curves for different fiber/matrix interface shear stress and interface debonding energy are shown in Figures 3 and 4. When the fiber/matrix interface shear stress increases, the matrix cracking density, saturation matrix cracking stress, and the interface debonding length increase;

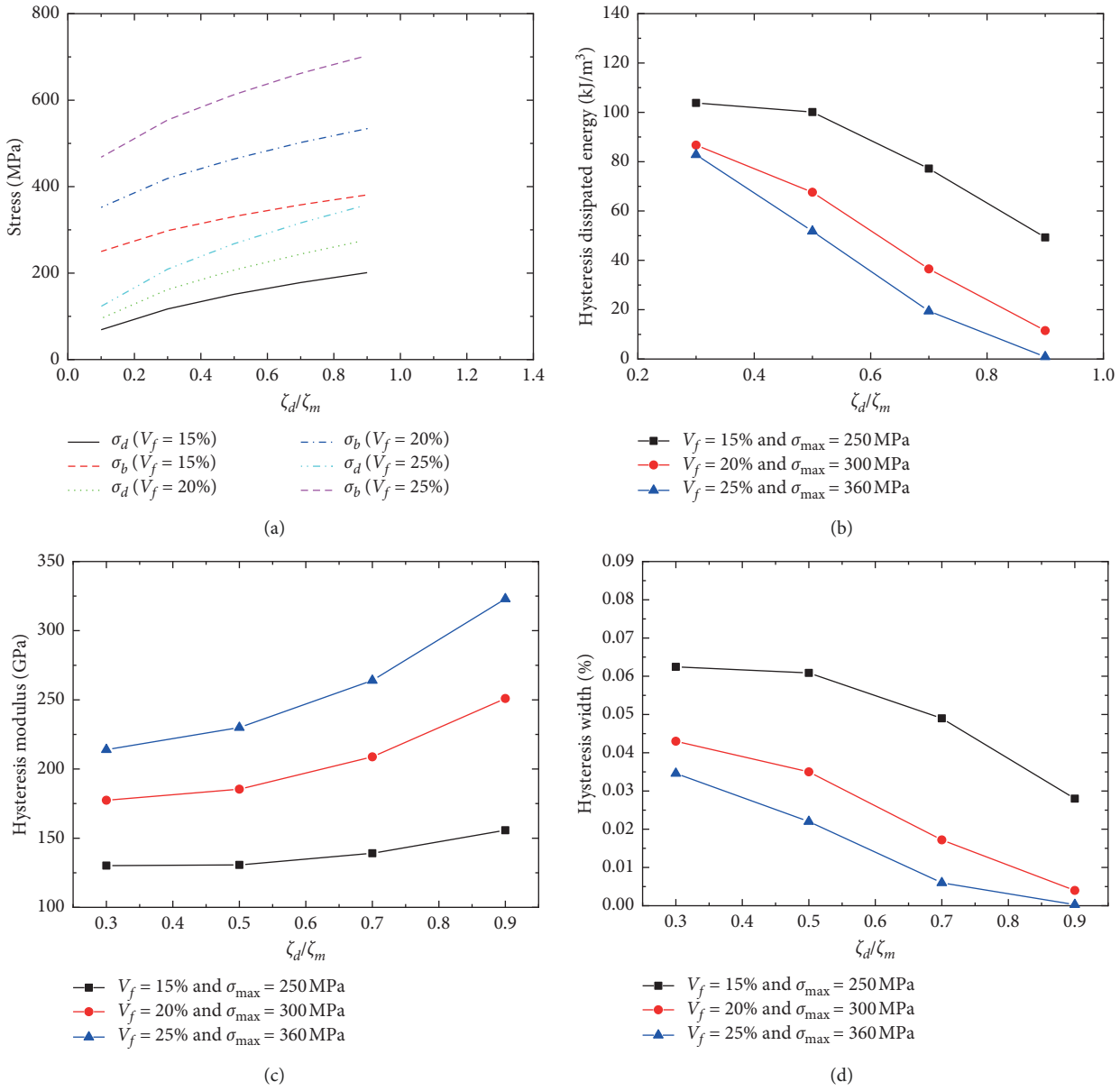

Figure 6: (a) The initial interface debonding stress and complete interface debonding stress versus the interface debonding energy curves; (b) the fatigue hysteresis dissipated energy versus the interface debonding energy curves; (c) the fatigue hysteresis modulus versus the interface debonding energy curves; (d) the fatigue hysteresis width versus the interface debonding energy curves for different fiber volume.

Table 1: Material properties of 2D SiC/SiC composites.

Items	Hi-Nicalon™ SiC/SiC	Sylramic™ SiC/SiC	Tyranno™ SiC/SiC
r_f (μm)	7	5	5.5
V_f (%)	14–18	12–21	29
E_f (GPa)	270	310	170
E_m (GPa)	350	350	350
α_f (10^{-6}/°C)	3.5	5.4	4
α_m (10^{-6}/°C)	4.6	4.6	4.6
σ_c (GPa)	3	2.6	1.9
m	5	5	5

and when the interface debonding energy increases, the matrix cracking density decreases, and the saturation matrix cracking stress increases.

When the fiber/matrix interface shear stress is $\tau_i = 20$ MPa, the matrix cracking density increases from $\lambda = 0.09$/mm at $\sigma_{mc} = 155$ MPa to $\lambda = 2.5$/mm at

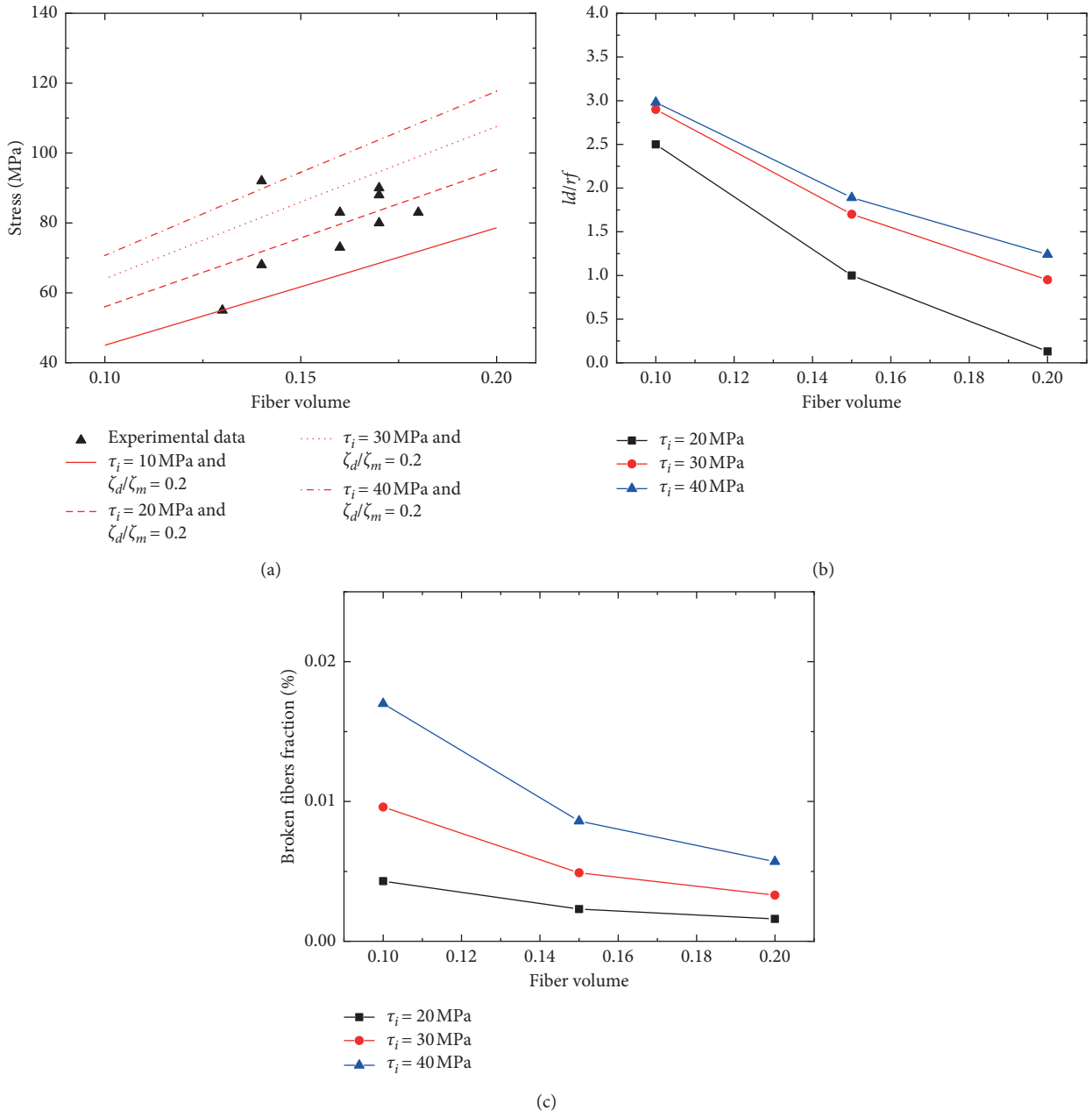

FIGURE 7: (a) The experimental and predicted first matrix cracking stress versus the fiber volume curves; (b) the interface debonding length versus the fiber volume curves; (c) the broken fibers fraction versus the fiber volume curves of 2D Hi-Nicalon™ SiC/SiC composite.

$\sigma_{sat} = 230$ MPa; the fiber/matrix interface debonding length increases from $2l_d/l_c = 0.9\%$ at $\sigma_{mc} = 155$ MPa to $2l_d/l_c = 60.8\%$ at $\sigma_{sat} = 230$ MPa; and the broken fibers fraction increases from $q = 0.169\%$ at $\sigma_{mc} = 155$ MPa to $q = 2\%$ at $\sigma_{sat} = 230$ MPa. When the fiber/matrix interface shear stress is $\tau_i = 40$ MPa, the matrix cracking density increases from $\lambda = 0.13$/mm at $\sigma_{mc} = 178$ MPa to $\lambda = 3.9$/mm at $\sigma_{sat} = 267$ MPa; the fiber/matrix interface debonding length increases from $2l_d/l_c = 0.96\%$ at $\sigma_{mc} = 178$ MPa to $2l_d/l_c = 63.4\%$ at $\sigma_{sat} = 267$ MPa; and the broken fibers fraction increases from $q = 0.38\%$ at $\sigma_{mc} = 178$ MPa to $q = 4.9\%$ at $\sigma_{sat} = 267$ MPa.

When the fiber/matrix interface debonding energy is $\zeta_d/\zeta_m = 0.1$, the matrix cracking density increases from $\lambda = 0.1$/mm at $\sigma_{mc} = 149$ MPa to $\lambda = 3.5$/mm at $\sigma_{sat} = 240$ MPa; the fiber/matrix interface debonding length increases from $2l_d/l_c = 1\%$ at $\sigma_{mc} = 149$ MPa to $2l_d/l_c = 72\%$ at $\sigma_{sat} = 240$ MPa; and the broken fibers fraction increases from $q = 0.1\%$ at $\sigma_{mc} = 149$ MPa to $q = 2.4\%$ at $\sigma_{sat} = 240$ MPa. When the fiber/matrix interface debonding energy is $\zeta_d/\zeta_m = 0.5$, the matrix cracking density increases from $\lambda = 0.13$/mm at $\sigma_{mc} = 208$ MPa to $\lambda = 2.7$/mm at $\sigma_{sat} = 280$ MPa; the fiber/matrix interface debonding length increases from $2l_d/l_c = 0.8\%$ at $\sigma_{mc} = 208$ MPa to $2l_d/l_c = 47\%$ at $\sigma_{sat} = 280$ MPa;

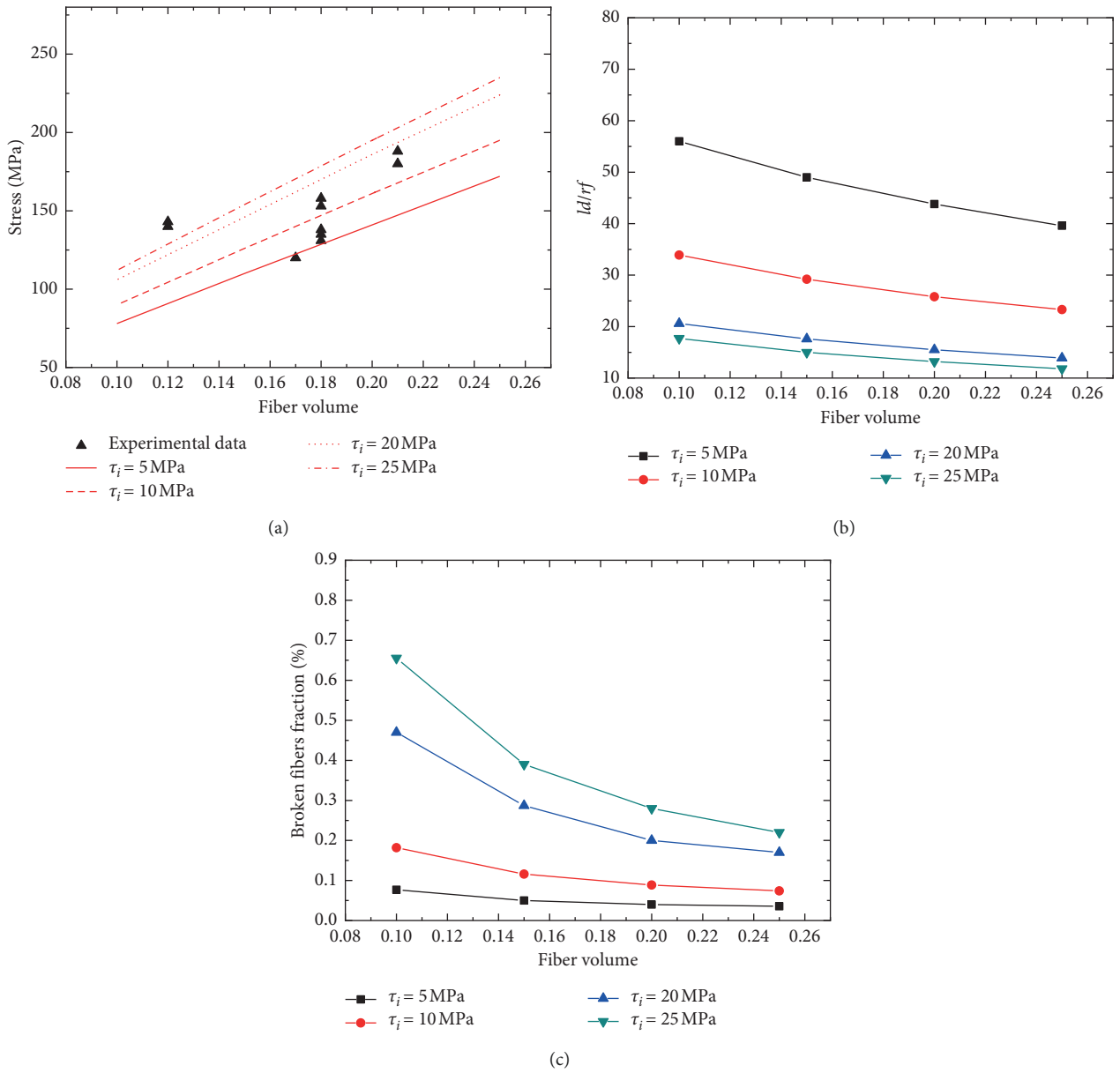

Figure 8: (a) The experimental and predicted first matrix cracking stress versus the fiber volume curves; (b) the interface debonding length versus the fiber volume curves; (c) the broken fibers fraction versus the fiber volume curves of 2D Sylramic™ SiC/SiC composite.

and the broken fibers fraction increases from $q = 1\%$ at $\sigma_{mc} = 208$ MPa to $q = 7\%$ at $\sigma_{\text{sat}} = 280$ MPa.

3.3. Effect of the Interface Properties on the Fatigue Hysteresis-Based Damage Parameters. The initial fiber/matrix interface debonding stress and the complete interface debonding stress, fatigue hysteresis dissipated energy, fatigue hysteresis modulus, and fatigue hysteresis width versus the fiber/matrix interface shear stress and interface debonding energy curves for different fiber volume are shown in Figures 5 and 6. When the fiber/matrix interface shear stress and the interface debonding energy increase, the initial interface debonding stress and the complete interface debonding stress increase, the fatigue hysteresis dissipated energy decreases, the fatigue hysteresis modulus increases, and the fatigue hysteresis width decreases.

When the fiber volume is $V_f = 15\%$, the initial fiber/matrix interface debonding stress increases from $\sigma_d = 95$ MPa at $\tau_i = 20$ MPa to $\sigma_d = 98$ MPa at $\tau_i = 40$ MPa and from $\sigma_d = 69$ MPa at $\zeta_d/\zeta_m = 0.1$ to $\sigma_d = 201$ MPa at $\zeta_d/\zeta_m = 0.9$; the complete fiber/matrix interface debonding stress increases from $\sigma_b = 215$ MPa at $\tau_i = 20$ MPa to $\sigma_b = 338$ MPa at $\tau_i = 40$ MPa and from $\sigma_b = 250$ MPa at $\zeta_d/\zeta_m = 0.1$ to $\sigma_b = 381$ MPa at $\zeta_d/\zeta_m = 0.9$; when the fatigue peak stress is $\sigma_{\max} = 150$ MPa, the fatigue hysteresis dissipated energy decreases from $U_e = 29.1$ kJ/m^3 at $\tau_i = 20$ MPa to $U_e = 15.4$ kJ/m^3 at $\tau_i = 40$ MPa; the fatigue hysteresis modulus increases from $E = 143$ GPa at $\tau_i = 20$ MPa to $E = 202$ GPa at $\tau_i = 40$ MPa; and the fatigue hysteresis width

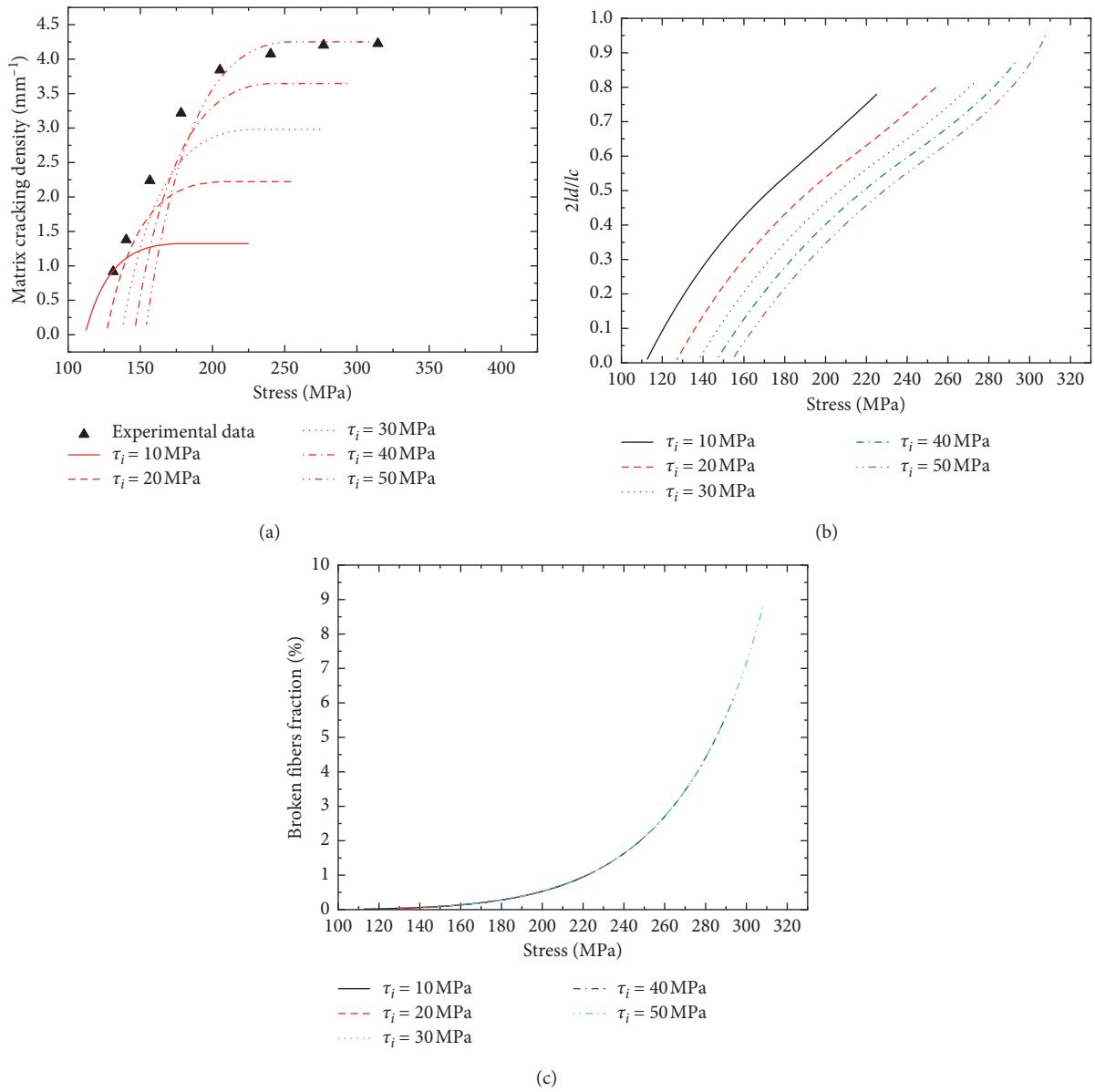

FIGURE 9: (a) The experimental and predicted matrix cracking density versus the applied stress curves; (b) the interface debonding length versus the applied stress curves; (c) the broken fibers fraction versus the applied stress curves of 2D Hi-Nicalon™ SiC/SiC composite.

decreases from $\Delta\varepsilon = 0.03\%$ at $\tau_i = 20$ MPa to $\Delta\varepsilon = 0.015\%$ at $\tau_i = 40$ MPa; when the fatigue peak stress is $\sigma_{max} = 250$ MPa, the fatigue hysteresis dissipated energy decreases from $U_e = 103.8$ kJ/m^3 at $\zeta_d/\zeta_m = 0.3$ to $U_e = 49.3$ kJ/m^3 at $\zeta_d/\zeta_m = 0.9$; the fatigue hysteresis modulus increases from $E = 130$ GPa at $\zeta_d/\zeta_m = 0.3$ to $E = 155$ GPa at $\zeta_d/\zeta_m = 0.9$; and the fatigue hysteresis width decreases from $\Delta\varepsilon = 0.06\%$ at $\zeta_d/\zeta_m = 0.3$ to $\Delta\varepsilon = 0.028\%$ at $\zeta_d/\zeta_m = 0.9$.

When the fiber volume is $V_f = 20\%$, the initial fiber/matrix interface debonding stress increases from $\sigma_d = 131$ MPa at $\tau_i = 20$ MPa to $\sigma_d = 135$ MPa at $\tau_i = 40$ MPa and from $\sigma_d = 95$ MPa at $\zeta_d/\zeta_m = 0.1$ to $\sigma_d = 277$ MPa at $\zeta_d/\zeta_m = 0.9$; the complete fiber/matrix interface debonding stress increases from $\sigma_b = 303$ MPa at $\tau_i = 20$ MPa to $\sigma_b = 477$ MPa at $\tau_i = 40$ MPa and from $\sigma_b = 352$ MPa at $\zeta_d/\zeta_m = 0.1$ to $\sigma_b = 534$ MPa at $\zeta_d/\zeta_m = 0.9$; when the fatigue peak stress is $\sigma_{max} = 150$ MPa, the fatigue hysteresis dissipated energy decreases from $U_e = 3.9$ kJ/m^3 at $\tau_i = 20$ MPa to $U_e = 2.1$ kJ/m^3 at $\tau_i = 40$ MPa; the fatigue hysteresis modulus increases from $E = 251$ GPa at $\tau_i = 20$ MPa to $E = 289$ GPa at $\tau_i = 40$ MPa; and the fatigue hysteresis width decreases from $\Delta\varepsilon = 0.003\%$ at $\tau_i = 20$ MPa to $\Delta\varepsilon = 0.0017\%$ at $\tau_i = 40$ MPa; when the fatigue peak stress is $\sigma_{max} = 300$ MPa, the fatigue hysteresis dissipated energy decreases from $U_e = 86.7$ kJ/m^3 at $\zeta_d/\zeta_m = 0.3$ to $U_e = 11.5$ kJ/m^3 at $\zeta_d/\zeta_m = 0.9$; the fatigue hysteresis modulus increases from $E = 177$ GPa at $\zeta_d/\zeta_m = 0.3$

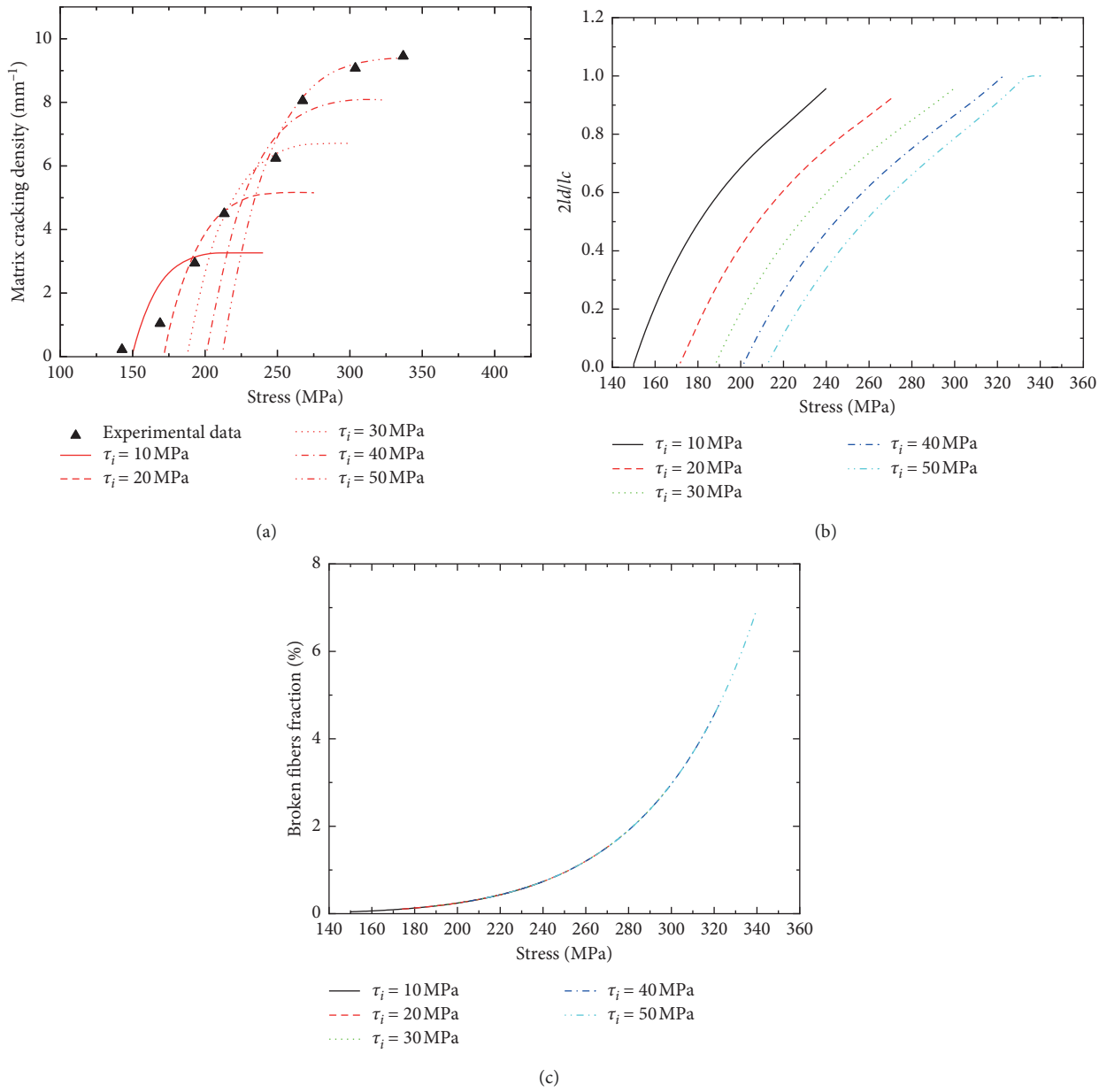

FIGURE 10: (a) The experimental and predicted matrix cracking density versus the applied stress curves; (b) the interface debonding length versus the applied stress curves; (c) the broken fibers fraction versus the applied stress curves of 2D Sylramic™ SiC/SiC composite.

to $E = 251$ GPa at $\zeta_d/\zeta_m = 0.9$; and the fatigue hysteresis width decreases from $\Delta\varepsilon = 0.043\%$ at $\zeta_d/\zeta_m = 0.3$ to $\Delta\varepsilon = 0.004\%$ at $\zeta_d/\zeta_m = 0.9$.

4. Experimental Comparisons

Morscher et al. [36–38] performed the experimental investigations on the first matrix cracking stress, matrix cracking evolution, and fatigue hysteresis loops of 2D SiC/SiC composites. The first matrix cracking stress, matrix cracking density, and the fatigue hysteresis loops of 2D Hi-Nicalon™, Sylramic™, and Tyranno™ SiC/SiC composites are predicted. The material properties of SiC/SiC composites are listed in Table 1.

4.1. First Matrix Cracking Stress. The experimental and predicted first matrix cracking stress versus the fiber volume curves of 2D Hi-Nicalon™ SiC/SiC composite for different fiber/matrix interface shear stress curves is shown in Figure 7. The fiber/matrix interface shear stress is in the range of $\tau_i = 10$–40 MPa at the interface debonding energy of $\zeta_d/\zeta_m = 0.2$. The first matrix cracking stress increases with the fiber volume and the interface shear stress; the interface debonding length decreases with the fiber volume and increases with the interface shear stress; and the broken fibers fraction decreases with the fiber volume and increases the interface shear stress.

The experimental and predicted first matrix cracking stress versus the fiber volume curves of 2D Sylramic™ SiC/

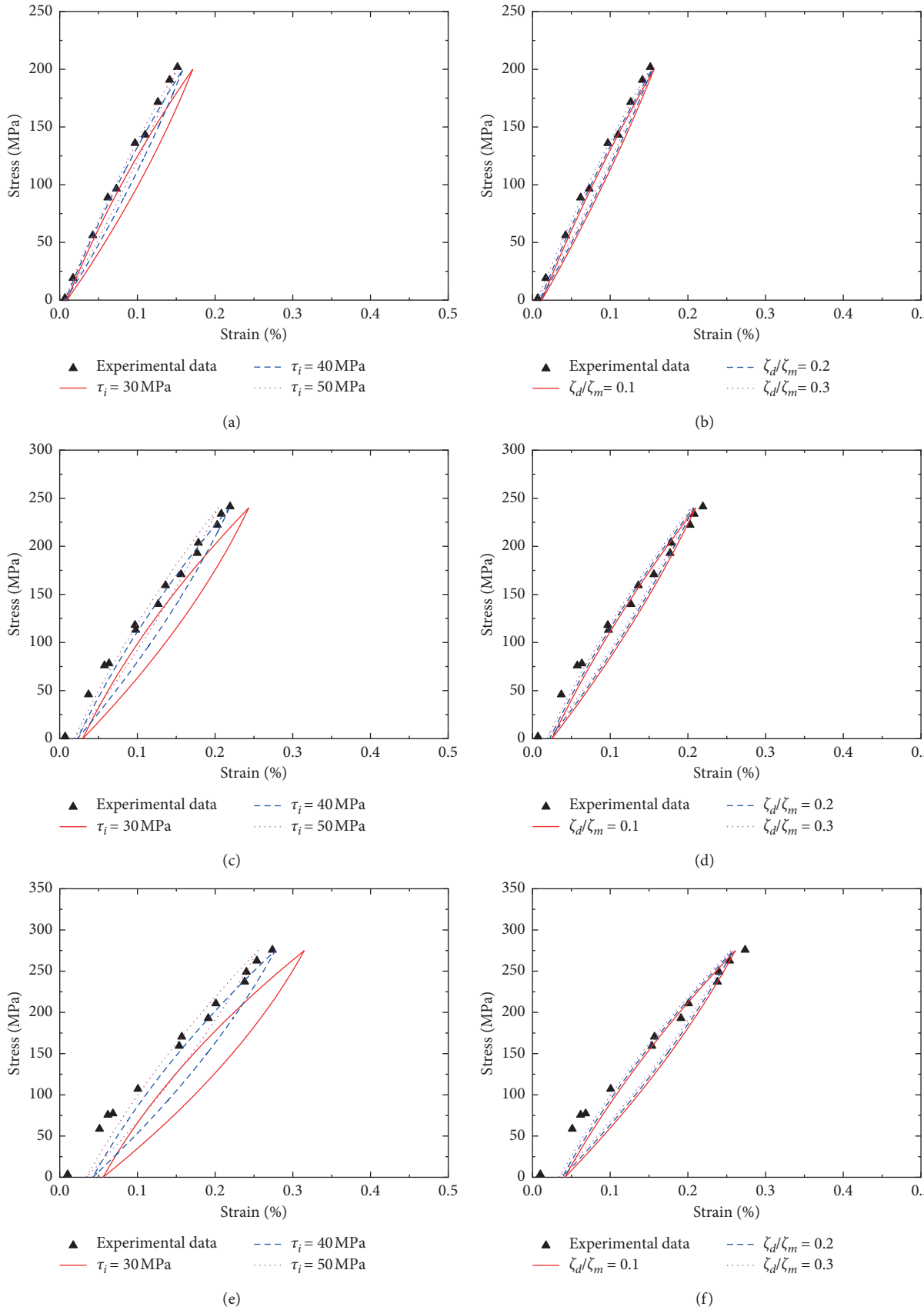

FIGURE 11: The experimental and predicted hysteresis loops of 2D Sylramic™ SiC/SiC composite under (a) the fatigue peak stress of $\sigma_{max} = 200$ MPa for different interface shear stress; (b) the fatigue peak stress of $\sigma_{max} = 200$ MPa for different interface debonding energy; (c) the fatigue peak stress of $\sigma_{max} = 240$ MPa for different interface shear stress; (d) the fatigue peak stress of $\sigma_{max} = 240$ MPa for different interface debonding energy; (e) the fatigue peak stress of $\sigma_{max} = 275$ MPa for different interface shear stress; (f) the fatigue peak stress of $\sigma_{max} = 275$ MPa for different interface debonding energy.

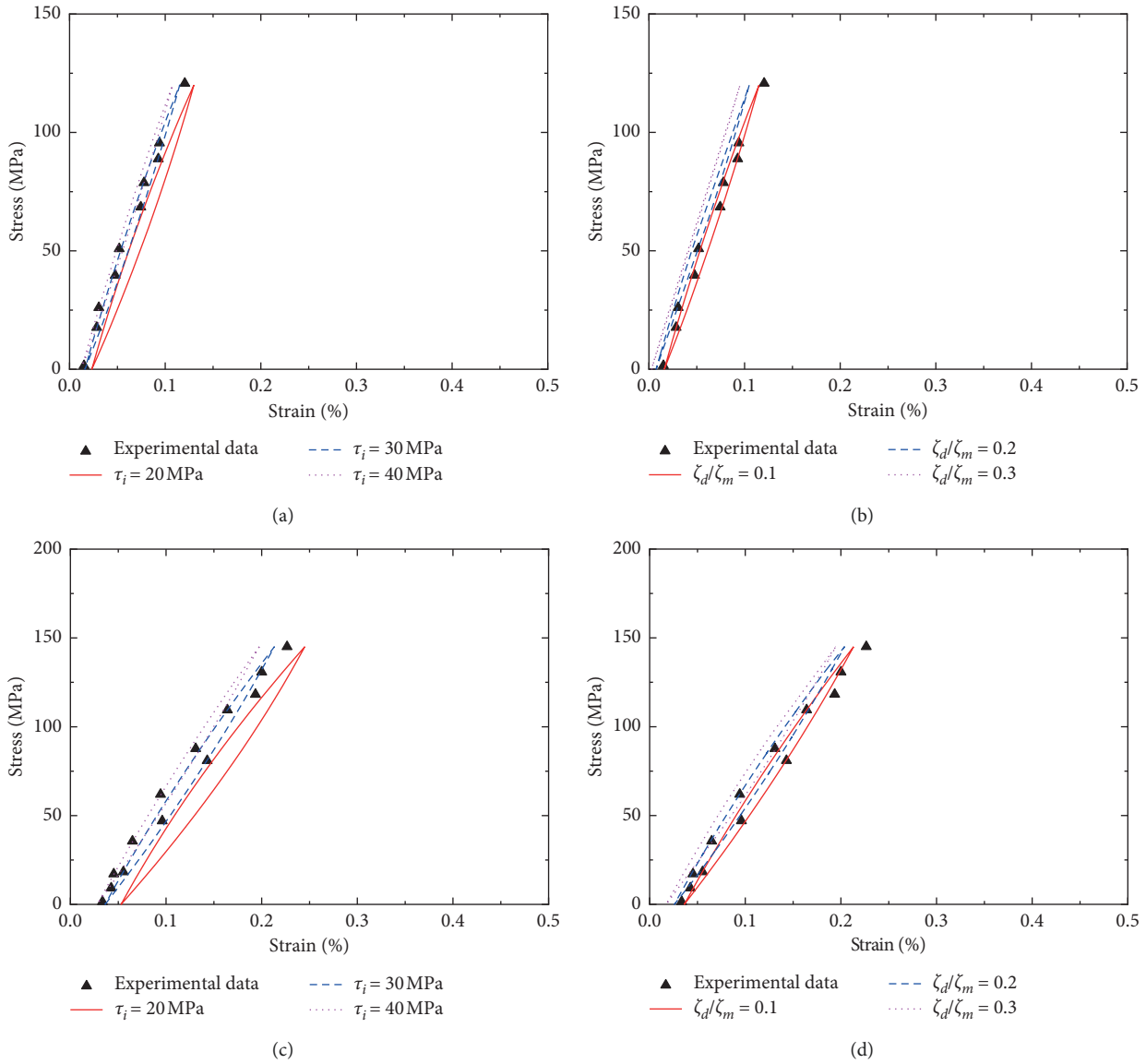

FIGURE 12: The experimental and predicted fatigue hysteresis loops of 2D Tyranno™ SiC/SiC composite under (a) the fatigue peak stress of $\sigma_{max} = 120$ MPa for different interface shear stress; (b) the fatigue peak stress of $\sigma_{max} = 120$ MPa for different interface debonding energy; (c) the fatigue peak stress of $\sigma_{max} = 145$ MPa for different interface shear stress; (d) the fatigue peak stress of $\sigma_{max} = 145$ MPa for different interface debonding energy.

SiC composite for different interface shear stress curves is shown in Figure 8. The interface shear stress is in the range of $\tau_i = 5$–25 MPa at the interface debonding energy of $\zeta_d/\zeta_m = 0.1$. The first matrix cracking stress increases with the fiber volume and the interface shear stress; the interface debonding length decreases with the fiber volume and the interface shear stress; and the broken fibers fraction decreases the fiber volume and increases with the interface shear stress.

4.2. Matrix Cracking Density. The experimental and predicted matrix cracking density versus the applied stress curves for different interface shear stress of 2D Hi-Nicalon™ SiC/SiC composite is shown in Figure 9. When the interface shear stress is low, the first matrix cracking stress, matrix cracking saturation stress, and saturation matrix cracking density are low. For the initial stage of matrix cracking evolution, the predicted result using low interface shear stress of $\tau_i = 20$ MPa agreed with experimental data; however, for the stage of matrix cracking evolution at high stress, the predicted results using high interface shear stress of $\tau_i = 50$ MPa agreed with experimental data. During matrix cracking evolution, the fiber/matrix interface debonding length and broken fibers fraction increase.

The experimental and predicted matrix cracking density versus the applied stress curves for different interface shear stress of 2D Sylramic™ SiC/SiC composite is shown in Figure 10. For the initial stage of matrix cracking evolution, the predicted result using the low interface shear stress of

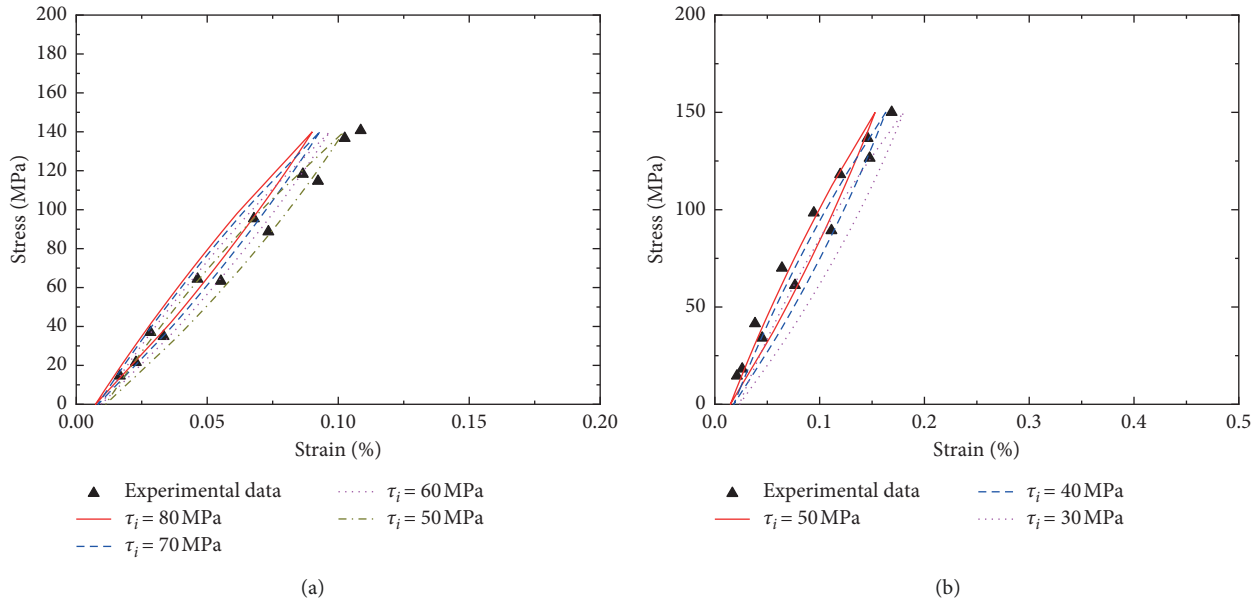

FIGURE 13: The experimental and predicted fatigue hysteresis loops of 2D Hi-Nicalon™ SiC/SiC composite under (a) the fatigue peak stress of $\sigma_{max} = 140$ MPa for $N = 13000$ cycles and (b) the fatigue peak stress of $\sigma_{max} = 150$ MPa for $N = 27000$ cycles.

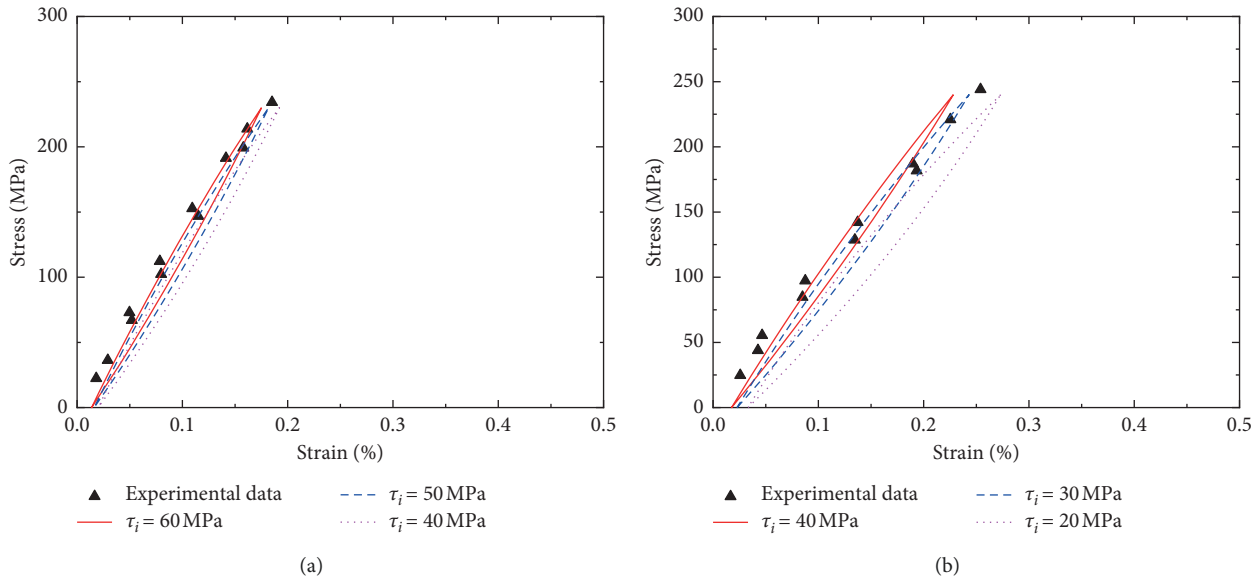

FIGURE 14: The experimental and predicted fatigue hysteresis loops of 2D Tyranno™ SiC/SiC composite under (a) the fatigue peak stress of $\sigma_{max} = 230$ MPa for $N = 16000$ cycles and (b) the fatigue peak stress of $\sigma_{max} = 240$ MPa for $N = 85$ cycles.

$\tau_i = 10$ and 20 MPa agreed with experimental data; however, for the stage of matrix cracking evolution at high stress, the predicted results using the high interface shear stress of $\tau_i = 50$ MPa agreed with experimental data. Under tensile loading, the interface debonding length increases after saturation of matrix cracking, and the fiber failure occurs at first matrix cracking stress.

4.3. Fatigue Hysteresis-Based Damage Parameters. The experimental and predicted hysteresis loops of 2D Sylramic™ SiC/SiC composite under the fatigue peak stresses of $\sigma_{max} = 200$, 240, and 275 MPa for different interface properties are shown in Figure 11. When the fatigue peak stress is $\sigma_{max} = 200$, 240, and 275 MPa, the predicted fatigue hysteresis loops for the interface shear stress of $\tau_i = 30$, 40, and 50 MPa and the interface debonding energy of $\zeta_d/\zeta_m = 0.1$, 0.2, and 0.3 are shown in Figure 11. The predicted results using the interface shear stress of $\tau_i = 50$ MPa and $\zeta_d/\zeta_m = 0.3$ agreed with the experimental hysteresis loops.

The experimental and predicted hysteresis loops of 2D Tyranno™ SiC/SiC composite under the fatigue peak stress of $\sigma_{max} = 120$ and 145 MPa for different interface properties

are shown in Figure 12. When the fatigue peak stress is $\sigma_{max} = 120$ and 145 MPa, the predicted fatigue hysteresis loops for the interface shear stress of $\tau_i = 20$, 30, and 40 MPa and the interface debonding energy of $\zeta_d/\zeta_m = 0.1$, 0.2, and 0.3 is shown in Figure 12. The predicted results using the interface shear stress of $\tau_i = 30$ MPa and $\zeta_d/\zeta_m = 0.1$ agreed with the experimental hysteresis loops.

The fatigue hysteresis loops of 2D Hi-Nicalon™ SiC/SiC composite under the fatigue peak stress of $\sigma_{max} = 140$ and 150 MPa are shown in Figure 13. When the fatigue peak stress is $\sigma_{max} = 140$ MPa, the experimental and predicted fatigue hysteresis loops using the interface shear stress of $\tau_i = 50$, 60, 70, and 80 MPa are shown in Figure 13(a), in which the predicted fatigue hysteresis loops with $\tau_i = 50$ MPa agreed with experimental data; when the fatigue peak stress is $\sigma_{max} = 150$ MPa, the experimental and predicted fatigue hysteresis loops using the interface shear stress of $\tau_i = 30$, 40, and 50 MPa are shown in Figure 13(b), in which the predicted fatigue hysteresis loops with $\tau_i = 40$ MPa agreed with experimental data. Under cyclic fatigue loading, the interface wear leads to the degradation of the interface shear stress.

The fatigue hysteresis loops of 2D Tyranno™ SiC/SiC composite under the fatigue peak stress of $\sigma_{max} = 230$ and 240 MPa are shown in Figure 14. When the fatigue peak stress is $\sigma_{max} = 230$ MPa, the experimental and predicted fatigue hysteresis loops using the interface shear stress of $\tau_i = 40$, 50, and 60 MPa are shown in Figure 14(a), in which the predicted fatigue hysteresis loops with $\tau_i = 50$ MPa agreed with experimental data; when the fatigue peak stress is $\sigma_{max} = 240$ MPa, the experimental and predicted fatigue hysteresis loops using the interface shear stress of $\tau_i = 20$, 30, and 40 MPa are shown in Figure 14(b), in which the predicted hysteresis loops with $\tau_i = 30$ MPa agreed with experimental data. Under repeated loading/unloading, the interface shear stress decreases due to the interface wear.

5. Conclusions

In this paper, the effect of the fiber/matrix interface properties on the tensile and fatigue behavior of 2D SiC/SiC composites was investigated. The relationships between the interface properties and the composite tensile and fatigue damage were established. The effects of the fiber/matrix interface properties on the first matrix cracking stress, matrix cracking evolution, first and complete interface debonding stress, fatigue hysteresis dissipated energy, fatigue hysteresis modulus, and fatigue hysteresis width were analyzed. The experimental first matrix cracking stress, matrix cracking evolution, and fatigue hysteresis loops of 2D SiC/SiC composites were predicted using different interface properties:

(1) When the interface shear stress increases, the first matrix cracking stress increases and the broken fibers fraction increases; the matrix cracking density, the saturation matrix cracking stress, and the interface debonding length increase; the initial interface debonding stress and the complete interface debonding stress increase, the hysteresis dissipated energy decreases, the hysteresis modulus increases, and the hysteresis width decreases.

(2) When the interface debonding energy increases, the first matrix cracking stress increases and the broken fibers fraction increases; the matrix cracking density decreases and the saturation matrix cracking stress increases; and the initial interface debonding stress and the complete interface debonding stress increase, the hysteresis dissipated energy decreases, the hysteresis modulus increases, and the hysteresis width decreases.

Data Availability

The data used to support the findings of this study are available from the corresponding author upon request.

Conflicts of Interest

The author declares that there are no conflicts of interest.

Acknowledgments

The work reported here was supported by the Fundamental Research Funds for the Central Universities (Grant no. NS2019038).

References

[1] R. Naslain, "Design, preparation and properties of non-oxide CMCs for application in engines and nuclear reactors: an overview," *Composites Science and Technology*, vol. 64, no. 2, pp. 155–170, 2004.

[2] J. A. DiCarlo and M. van Roode, "Ceramic composite development for gas turbine hot section components," in *Proceedings of the Volume 2: Aircraft Engine; Ceramics; Coal, Biomass and Alternative Fuels; Controls, Diagnostics and Instrumentation; Environmental and Regulatory Affairs*, Barcelona, Spain, 2006.

[3] J. A. DiCarlo, H. M. Yun, G. N. Morscher, and R. T. Bhatt, "SiC/SiC composites for 1200°C and above," in *Handbook of Ceramic Composites*, N. P. Bansal, Ed., Springer, Boston, MA, USA, 2005.

[4] F. W. Zok, "Ceramic-matrix composites enable revolutionary gains in turbine engine efficiency," *American Ceramic Society Bulletin*, vol. 95, pp. 22–28, 2016.

[5] F. J. Lino Alves, A. M. Baptista, and A. T. Marques, "Metal and ceramic matrix composites in aerospace engineering," in *Advanced Composite Materials for Aerospace Engineering Processing, Properties and Applications*, S. Rana and R. Fangueiro, Eds., Woodhead Publishing, Sawston, UK, 2016.

[6] L. Li, *Damage, Fracture and Fatigue of Ceramic-Matrix Composites*, Springer Nature Singapore Pte Ltd., Singapore, 2018.

[7] R. R. Naslain, "SiC-matrix composites: nonbrittle ceramics for thermo-structural application," *International Journal of Applied Ceramic Technology*, vol. 2, no. 2, pp. 75–84, 2005.

[8] M. C. Halbig, M. H. Jaskowiak, J. D. Kiser, and D. Zhu, "Evaluation of ceramic matrix composite technology for aircraft turbine engine applications," NASA Report, NASA, Washington, DC, USA, 2013.

[9] D. Ding, "Processing, properties and applications of ceramic matrix composites, SiC/SiC: an overview," in *Advances in Ceramic Matrix Composites*, I. M. Low, Ed., Woodhead Publishing, Sawston, UK, 2014.

[10] F. Watanabe and T. Manabe, "Engine testing for the demonstration of a 3D-woven based ceramic matrix composite turbine vane design concept," in *Proceedings of the Volume 6: Ceramics; Controls, Diagnostics, and Instrumentation; Education; Manufacturing Materials and Metallurgy*, Oslo, Norway, June 2018.

[11] R. S. Kumar, M. Mordasky, and G. Ojard, "Delamination fracture in ceramic matrix composites: from coupons to components," in *Proceedings of the Volume 6: Ceramics; Controls, Diagnostics, and Instrumentation; Education; Manufacturing Materials and Metallurgy*, Oslo, Norway, June 2018.

[12] C. D. Newton, J. P. Jones, L. Gale, and M. R. Bache, "Detection of strain and damage distribution in SiC/SiC mechanical test coupons," in *Proceedings of the Volume 6: Ceramics; Controls, Diagnostics, and Instrumentation; Education; Manufacturing Materials and Metallurgy*, Oslo, Norway, June 2018.

[13] F. Rebillat, "Advances in self-healing ceramic matrix composites," in *Advances in Ceramic Matrix Composites*, I. M. Low, Ed., Woodhead Publishing, Sawston, UK, 2014.

[14] Z. Xia and L. Li, "Understanding interfaces and mechanical properties of ceramic matrix composites," in *Advances in Ceramic Matrix Composites*, I. M. Low, Ed., Woodhead Publishing, Sawston, UK, 2014.

[15] L. B. Li, Y. D. Song, and Y. C. Sun, "Modeling the tensile behavior of unidirectional C/SiC ceramic-matrix composites," *Mechanics of Composite Materials*, vol. 49, no. 6, pp. 659–672, 2014.

[16] L. B. Li, Y. D. Song, and Y. C. Sun, "Modeling the tensile behavior of cross-ply C/SiC ceramic-matrix composites," *Mechanics of Composite Materials*, vol. 51, no. 3, pp. 359–376, 2015.

[17] L. B. Li, "Modeling the monotonic and cyclic tensile stress-strain behavior of 2D and 2.5D woven C/SiC ceramic-matrix composites," *Mechanics of Composite Materials*, vol. 54, no. 2, pp. 165–178, 2018.

[18] L. Li, "A thermomechanical fatigue hysteresis-based damage evolution model for fiber-reinforced ceramic-matrix composites," *International Journal of Damage Mechanics*, vol. 28, no. 3, pp. 380–403, 2019.

[19] L. Li, "Micromechanics modeling of fatigue hysteresis behavior in carbon fiber-reinforced ceramic-matrix composites. Part I: theoretical analysis," *Composites Part B: Engineering*, vol. 159, pp. 502–513, 2019.

[20] L. Li, "Damage and fracture of fiber-reinforced ceramic-matrix composites under thermal fatigue loading in oxidizing atmosphere," *Journal of the Ceramic Society of Japan*, vol. 127, no. 2, pp. 67–80, 2019.

[21] E. Vagaggini, J.-M. Domergue, and A. G. Evans, "Relationships between hysteresis measurements and the constituent properties of ceramic matrix composites: I, theory," *Journal of the American Ceramic Society*, vol. 78, no. 10, pp. 2709–2720, 1995.

[22] J.-M. Domergue, E. Vagaggini, and A. G. Evans, "Relationship between hysteresis measurements and the constituent properties of ceramic matrix composites: II, experimental studies on unidirectional materials," *Journal of the American Ceramic Society*, vol. 78, no. 10, pp. 2721–2731, 1995.

[23] W. A. Curtin, B. K. Ahn, and N. Takeda, "Modeling brittle and tough stress-strain behavior in unidirectional ceramic matrix composites," *Acta Materialia*, vol. 46, no. 10, pp. 3409–3420, 1998.

[24] N. Carrère, E. Martin, and J. Lamon, "The influence of the interphase and associated interfaces on the deflection of matrix cracks in ceramic matrix composites," *Composites Part A: Applied Science and Manufacturing*, vol. 31, no. 11, pp. 1179–1190, 2000.

[25] Z. Xia and W. A. Curtin, "Tough-to-brittle transitions in ceramic-matrix composites with increasing interfacial shear stress," *Acta Materialia*, vol. 48, no. 20, pp. 4879–4892, 2000.

[26] C. Sauder, A. Brusson, and J. Lamon, "Influence of interface characteristics on the mechanical properties of Hi-Nicalon type-S or Tyranno-SA3 fiber-reinforced SiC/SIC mini-composites," *International Journal of Applied Ceramic Technology*, vol. 7, no. 3, pp. 291–303, 2010.

[27] C. Cho, J. W. Holmes, and J. R. Barber, "Estimation of interfacial shear in ceramic composites from frictional heating measurements," *Journal of the American Ceramic Society*, vol. 74, no. 11, pp. 2802–2808, 1991.

[28] J. W. Holmes and C. Cho, "Experimental observation of frictional heating in fiber-reinforced ceramics," *Journal of the American Ceramic Society*, vol. 75, no. 4, pp. 929–938, 1992.

[29] A. G. Evans, F. W. Zok, and R. M. McMeeking, "Fatigue of ceramic matrix composites," *Acta Metallurgica et Materialia*, vol. 43, no. 3, pp. 859–875, 1995.

[30] P. Reynaud, "Cyclic fatigue of ceramic-matrix composites at ambient and elevated temperatures," *Composites Science and Technology*, vol. 56, no. 7, pp. 809–814, 1996.

[31] S. Zhu, M. Mizuno, Y. Kagawa, and Y. Mutoh, "Monotonic tension, fatigue and creep behavior of SiC-fiber-reinforced SiC-matrix composites: a review," *Composites Science and Technology*, vol. 59, no. 6, pp. 833–851, 1999.

[32] J. M. Staehler, S. Mall, and L. P. Zawada, "Frequency dependence of high-cycle fatigue behavior of CVI C/SiC at room temperature," *Composites Science and Technology*, vol. 63, no. 15, pp. 2121–2131, 2003.

[33] G. Fantozzi and P. Reynaud, "Mechanical hysteresis in ceramic matrix composites," *Materials Science and Engineering: A*, vol. 521-522, pp. 18–23, 2009.

[34] M. B. Ruggles-Wrenn, D. T. Christensen, A. L. Chamberlain, J. E. Lane, and T. S. Cook, "Effect of frequency and environment on fatigue behavior of a CVI SiC/SiC ceramic matrix composite at 1200°C," *Composites Science and Technology*, vol. 71, no. 2, pp. 190–196, 2011.

[35] K. G. Dassios, D. G. Aggelis, E. Z. Kordatos, and T. E. Matikas, "Cyclic loading of a SiC-fiber reinforced ceramic matrix composite reveals damage mechanisms and thermal residual stress state," *Composites Part A: Applied Science and Manufacturing*, vol. 44, pp. 105–113, 2013.

[36] G. Morscher, M. Singh, J. Kiser, M. Freedman, and R. Bhatt, "Modeling stress-dependent matrix cracking and stress-strain behavior in 2D woven SiC fiber reinforced CVI SiC composites," *Composites Science and Technology*, vol. 67, no. 6, pp. 1009–1017, 2007.

[37] G. N. Morscher, C. Baker, and C. Smith, "Electrical resistance of SiC fiber reinforced SiC/Si matrix composites at room temperature during tensile testing," *International Journal of Applied Ceramic Technology*, vol. 11, no. 2, pp. 263–272, 2014.

[38] Z. Han and G. N. Morscher, "Electrical resistance and acoustic emission during fatigue testing of SiC/SiC composites," in *Proceedings of the Mechanical Properties and Performance of Engineering Ceramics and Composites X: A Collection of Papers Presented at the 39th International Conference on Advanced Ceramics and Composites*, Daytona Beach, FL, USA, January 2015.